RESEARCH ARTICLE | MAY 12 2025

Pulse laser induced microbubble motion dynamic in a nanofluid pool *⊙*

Special Collection: Microfluidic Heat and Mass Transfer

Xin Yan (闫鑫) ☎ ⑩ ; Jinliang Xu (徐进良); Yuqian Zhang (张煜乾); Hongbiao Wang (王洪彪); Guohua Liu (刘国华) ⑩



Physics of Fluids 37, 052011 (2025) https://doi.org/10.1063/5.0272239





Articles You May Be Interested In

Experiments on the effects of nanoparticles on subcooled nucleate pool boiling

Physics of Fluids (May 2018)

Impacts of salt concentration on nucleate pool boiling of NaCl solution

AIP Advances (March 2023)

Simultaneous double droplet impact on a molten phase change material pool: An experimental investigation

Physics of Fluids (February 2023)





Pulse laser induced microbubble motion dynamic in a nanofluid pool

Cite as: Phys. Fluids **37**, 052011 (2025); doi: 10.1063/5.0272239 Submitted: 23 March 2025 · Accepted: 17 April 2025 · Published Online: 12 May 2025







Xin Yan (闫鑫),^{1,a)} <mark>向</mark> Jinliang Xu (徐进良),^{1,2} Yuqian Zhang (张煜乾),¹ Hongbiao Wang (王洪彪),¹ and Guohua Liu (刘国华)¹ 向

AFFILIATIONS

¹Beijing Key Laboratory of Multiphase Flow and Heat Transfer for Low Grade Energy Utilization, North China Electric Power University, Beijing, 102206, People's Republic of China

²Key Laboratory of Power Station Energy Transfer Conversion and System, North China Electric Power University, Ministry of Education, Beijing 102206, China

Note: This paper is part of the Special Topic, Microfluidic Heat and Mass Transfer.

^{a)}Author to whom correspondence should be addressed: yanxin@ncepu.edu.cn

ABSTRACT

Understanding bubbles motion dynamic with laser interaction is crucial for applications in boiling heat transfer enhancement, precision laser surgery, and cell manipulation. Here, we investigate the micro-bubbles motion dynamic with pulsed laser irradiation. A horizontally projected pulse laser induces the generation of vapor micro-bubbles in nanofluids via plasmonic absorption effects. Parametric variation in pulse energy and laser frequency reveals four distinct bubble flow regimes: (1) microbubble streaming, (2) frequency-regulated bubble orbital motion, (3) bubble self-rotation, and (4) bubble translation combined rotational motion. The frequency-regulated bubble orbital trajectory forms a triangular shape with oscillation amplitudes spanning 16.9–65.0 µm in the x-direction and 21.8–115.7 µm in the y-direction. The angular velocity of bubble self-rotation is about 13.2–20.3 rad/s. By force analysis, we identify Marangoni forces arising from thermal gradients and indirect light pressure resulting from asymmetric laser heating as dominant actuation mechanisms. At low frequencies, spatiotemporal characteristics of Marangoni forces enable bubble self-sustained orbital revolution. Conversely, high-frequency laser irradiation induces stationary bubble confined by Marangoni forces and buoyancy. The laser eccentrically irradiates the bubble, which induces indirect light pressure that drives the bubble's self-rotation. This study revolutionizes bubble motion manipulation by using pulsed lasers, thus enabling precise microfluidic operations. The introduction of laser-guided bubble motion can enhance heat transfer and facilitate advanced mixing and reagent management in chemical processes.

Published under an exclusive license by AIP Publishing. https://doi.org/10.1063/5.0272239

I. INTRODUCTION

Boiling is a high-efficient heat transfer process where the temperature of a liquid reaches its boiling point. As one of the crucial heat transfer mechanisms, the boiling process is applied in various fields, including power generation, chemical industry, materials manufacturing, and space industry. Numerous bubbles are generated on a hot solid surface or within the liquid, carrying away heat from the heated region. Therefore, controlling the behavior of bubbles is essential for enhancing the efficiency of boiling heat transfer. Many experimental investigations have been conducted to study the hydrodynamics of bubbles in pool boiling. However, studying bubble behavior presents significant challenges due to the randomness of bubble nucleation, the short timescales of bubble growth and departure, and the coupling between multiple physical fields. One way to address

these challenges and enable phenomenological analysis of boiling is to study the controlled single bubbles. Various external energy fields are employed to capture and manipulate bubbles, such as ultrasound, optical, magnetic, and electric fields. ^{10,11} The bubbles are confined within the potential well created by these energy fields. Among these methods, lasers offer a potentially flexible and controlled approach for generating and capturing bubbles. Lasers possess high energy flux and are widely used in material processing, ^{12–14} clinical treatments, ¹⁵ military applications, ¹⁶ and more.

The laser incident on a subcooling liquid pool can induce laser-induced breakdown cavitation and plasmonic bubbles. These are two different bubble cavitation mechanisms. When the incident laser irradiance exceeds the breakdown threshold of water, cavitation rapidly forms in the laser focal region.¹⁷ The pressure and temperature of the

cavitation can reach approximately 10³ MPa and 10⁴ K, respectively. The cavitation, which has high pressure, expands dramatically to form a bubble at supersonic speed leading to the shock wave propagation. Then the bubble continuously expands and collapses under the pressure gradient between the bubble and the surrounding water until the bubble's energy dissipates. During the bubble's rapid oscillation, huge energy is released into the surrounding liquid causing local jet flows, which have extensive applications in micro/nano-surgery, drug delivery, and tumor treatment. 22

The plasmonic bubbles originate from local heat deposition in liquid due to the photothermal conversion effect between the laser and the nanofluid.²³ Scholars have done a lot of work on the threshold of plasmon bubble generation and the influencing factors.^{24,25} Lombard *et al.*²⁵ conducted a series of experiments to study the process of micro/nanobubbles generation. The lifetime and maximum evolution radius of micro/nanobubbles are mainly controlled by ballistic heat flux, while the pump laser pulse width and energy density can affect the number of bubbles generated and the oscillation period. Lombard *et al.*²⁶ reported that the Laplace pressure, the contact angle of the solid-liquid interface, and interfacial thermal resistance play key roles in the liquid phase change around nanoparticles. Mohan *et al.*²⁷ suggested that the microbubbles come from the coalescence of nanobubbles initially formed around nanoparticles.

After the bubbles have stabilized in the liquid pool, the interaction between the bubbles and the laser causes the bubbles to exhibit different motion dynamic characteristics. Wei et al.²⁸ manipulated the bubble movement and separation processes achieved through thermal gradient-driven Marangoni effect under continuous laser irradiation. Li et al.²⁹ controlled the bubble anti-buoyancy motion by an intense Marangoni effect associated with non-uniform temperature distribution via focused continuous laser irradiation. However, as far as we know, there are few researchers who investigate the influence of pulse laser parameters on bubble dynamics and bubble flow patterns in liquid pools. The pulse laser has periodic phases of intense illumination and phases of no illumination, which introduce temporal variations in the temperature field, affecting the behavior of Marangoni forces and indirect light pressure. The Marangoni forces peak during the laser's ON phase and diminish during the OFF phase, showing significant spatial variations within and outside the laser beam. Indirect light pressure,³⁰ introduced by our research group, results from momentum transfer due to nonequilibrium vaporization at the bubble-liquid interface. It only affects bubble movement when the bubbles are within the laser beam during the ON phase. In addition, the effect of buoyancy is always acting on bubbles. Thus, the bubbles exhibit complex motion dynamics under the pulse laser irradiation.

In this study, we aim to investigate the effect of the pulse laser's parameters, such as single pulse energy (E_1) and frequency (f_1) , on the micro-bubble motion dynamic in a liquid pool. An experimental system was developed in which pulsed laser irradiation triggers plasmonic bubble nucleation in subcooled nanofluid. The hydrodynamics of these bubbles are studied using high-speed camera and infrared imaging. The force analysis acting on the bubbles reveals that the buoyancy, Marangoni forces, indirect light pressure are critical to the bubble motion dynamic characteristic. These forces interact in both horizontal and vertical directions, allowing the bubbles to behave distinct flow regimes. This study investigates the influence of pulsed laser parameters on the bubble dynamics in a liquid pool, offering a potential

bubble manipulation method in fields such as actuators, microscale heat exchange, micro-energy, and chemical engineering.

II. EXPERIMENT AND MATERIALS

A. Experiments

The experimental equipment was set up on an optical platform, as shown in Fig. 1(a). A pulsed laser with a wavelength of 527 nm was generated using a Nd laser device (PEGASUS PIV XR, New Wave). The laser's wavelength (527 nm) matches the resonance wavelength of the gold nanofluids, enhancing photothermal conversion and facilitating bubbles nucleation. The laser beam was focused using a convex lens with a focal length of 76 mm and directed toward the gold nanofluid. The beam width $d_{\rm l}$ and the cone angle of the focused laser are approximately 119 µm and 1.04°, respectively. Thus, the Rayleigh length $L_{\rm R}$ of the laser beam is 21.1 mm, which is larger than the width of the experimental observation region (\sim 2.8 mm). Therefore, it is assumed that the laser beam diameter remains constant within the observation region.

In this work, the gold nanofluid is used as the working fluid. The gold nanofluid (600 $\mu L)$ was placed in a $10\,mm \times 2\,mm \times 50\,mm$ quartz cuvette. The concentration was maintained at $100\,ppm$ to ensure rapid absorption of laser energy and to enable clear observation of phenomena within the fluid. The relative positions of the beam and cuvette were precisely controlled by a three-axis displacement

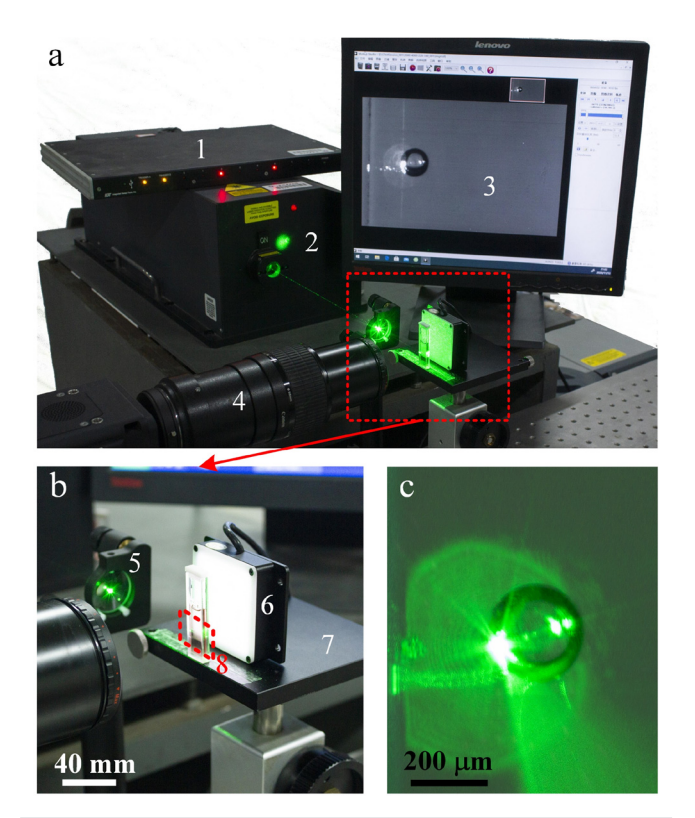


FIG. 1. Experimental setup. (a) 1, time synchronizer; 2, 527 nm pulse laser; 3, PC screen; and 4, high-speed camera. (b) 5, focusing lens; 6, back light; 7, three-axis displacement platform; 8, cuvette containing nanofluid. (c) Bubble observed due to onto the mal heating

platform. The spatial and temporal distributions of the temperature were measured using an infrared camera (InfraTec ImageIR 5380), which was corrected by a miniature precision thermocouple. The spatial resolution is 24 µm/pixel, and the temporal resolution is 5 ms. Prior to each experiment, the initial temperature of the gold nanofluid and the ambient temperature were both controlled at 20 ± 0.5 °C.

A high-speed camera (MotionPro Y4, IDT) was used to record the bubble characteristics within the nanofluid. To accurately reflect the bubble dynamics under laser irradiation, the laser and high-speed camera were synchronized via a timing controller. The spatial resolution of the high-speed camera was 2.71 µm/pixel with an adjustable frame rate f_r . The pulse frequency f_l and single-pulse energy E_l of the laser beam can be independently controlled. Due to the limitation of laser device, the f_1 was set between 50 and 2000 Hz, and E_1 ranged from 0.05 to 12.92 mJ. The average laser power P, depending on both the pulse frequency f_1 and single-pulse energy E_1 , was measured by a laser power meter (15(50) A-PH-DIF-18, OPHIR) with a measurement error of $\pm 5\%$. To ensure accurate observation of bubble motion within a single pulse cycle, the f_r was set as an integer multiple of the f_l .

The synchronization timing between the laser device and the high-speed camera was governed by four key parameters of the timing controller. They are the synchronous error δt_s =20 ns, the laser on delay δt_d =1 µs, the laser pulse duration time δt_l =180 ns, and the exposure time of the high-speed camera $\delta t_{\rm e}$ =200 μ s. The $\delta t_{\rm e}$ is at least two magnitudes larger than the sum of δt_s , δt_d , and δt_l , which ensure that the camera could capture the bubble motion during the laser ON and OFF phases. The details are illustrated in Ref. 30. Table S1 summarizes the experimental instruments, parameters, and their respective uncertainties. The uncertainties are from equipment manuals and calculated via error propagation methods. 32

B. Materials

Gold nanofluid exhibits high photothermal conversion efficiency in the visible light region, which is commonly used in solar energy photothermal conversion research.³³ When exposed to light at specific wavelengths, gold nanoparticles undergo plasmon resonance, enhancing light absorption and converting it into thermal energy, which causes bubbles generation.²³ The gold nanofluid in this study was synthesized via the sodium citrate reduction method. The characterization data are presented in Fig. S1. The gold nanoparticles are quasispherical with an average diameter $d_{p,ave} = 14.56$ nm. The spectral transmittance of a 100 ppm gold nanofluid sample was characterized using a UV-Vis spectrophotometer (Shimadzu UV-2550). As seen in Fig. S1c, the transmittance is lowest at $\lambda = 520$ nm, where the nanoparticles exhibit localized surface plasmon resonance (LSPR), maximizing light absorption and photothermal conversion. In this study, the laser wavelength used was 527 nm, closely matching 520 nm, which ensures strong light absorption by the nanofluid. To prevent impurities from influencing the bubble movement, all containers were rinsed with ultrapure water, and non-condensable gases were removed from the gold nanofluid by vacuum heating.

III. RESULTS AND DISCUSSION

A. Bubble flow regimes

With the laser heating, bubbles were generated in the gold nanofluid. The nanoparticles self-assemble on the bubble interface under various microscopic forces, enhancing the plasmonic effects and photothermal conversion. ³⁰ By varying the laser frequency f_1 and single pulse energy E_{l} , different bubble flow regimes were observed in subcooling nanofluid pool, as illustrated in Fig. 2. The bubble exhibits micro-bubble stream, periodic orbital motion, self-rotation, and oscillation characteristics within the liquid. Based on these characteristics, four flow regimes are identified, as shown in Table I.

In regime I, numerous micro-nanobubbles were trapped in the laser beam, moving rapidly to the right. In regime II, a micrometerscale bubble is generated, showing the periodic orbital motion with the laser ON and OFF. The centroid of the bubble traced a complete triangular path. The frequency of the motion matches the laser frequency f_1 . Regime III represents the limiting condition of the bubbles in regime II as the laser frequency increases. Here, a large bubble counterclockwise rotates quickly and smoothly. In regime IV, the bubble undergoes significant left-right oscillations driven by the laser while simultaneously self-rotating. The bubble oscillation frequency f_0 is significantly lower than the laser frequency f_1 .

Figure 3 illustrates the flow regime pattern map corresponding to different laser parameters, revealing a striped distribution pattern. As the single pulse energy E_1 increases, the bubble flow regime transitions from regime I to regime II (III) and finally to regime IV. In the intermediate striped zones, increasing the laser pulse frequency f₁ results in a transition from regime II to regime III. The black solid lines between the zones indicate the boundaries and transitions of bubble flow regimes. The following sections will provide detailed descriptions and analyses of each flow regime, considering the forces acting on the bubbles in the liquid.

B. The forces acting on the bubbles

A pulsed laser with a wavelength of 527 nm irradiating a gold nanofluid creates a spatiotemporal temperature field in the liquid pool. Additionally, photothermal conversion occurs at the bubble surfaces exposed to the laser irradiation, causing the bubbles to grow and evaporation momentum force.³⁰ Thus, in nanofluids, bubbles with laser irradiation experience four main forces: buoyancy F_b, Marangoni force F_{σ} , indirect light pressure F_{ν} and frictional drag $F_{\rm f}$. These forces vary with the bubble size, surrounding environment, motion state, and laser parameters. The imbalance forces acting on the bubble induced microbubble motion. The Marangoni force is related to the temperature field around bubble in liquid, which can be decomposed into vertical $F_{\sigma,y}$ and horizontal $F_{\sigma,x}$ components. Vertically, buoyancy F_b opposes the Marangoni force $F_{\sigma,y}$. If $F_{\sigma,y}$ exceeds F_b , the bubble moves toward the region with a higher temperature. Conversely, if buoyancy dominates, the bubble moves upwards. Horizontally, indirect light pressure F_i is balanced by the Marangoni force $F_{\sigma,x}$. When F_i governs the bubble movement, the bubble moves in the direction of laser beam propagation; otherwise, it moves under the effect of $F_{\sigma,x}$ to the warm region. The frictional drag F_f is passive force that is related to the motion of the bubbles. Due to the intermittent nature of pulsed laser irradiation, both the Marangoni force and indirect light pressure exhibit timevarying characteristics. These forces act together to drive bubble motion, resulting in diverse bubble flow regimes.

Buoyancy $F_{\rm b}$ arises from the density difference between the vapor inside the bubble and the surrounding liquid. It depends on the bubble volume V_b and is calculated as $F_b \approx 4\pi \rho_1 g r_b^3/3$, where ρ_l is the liquid density, and r_b is the bubble radius.

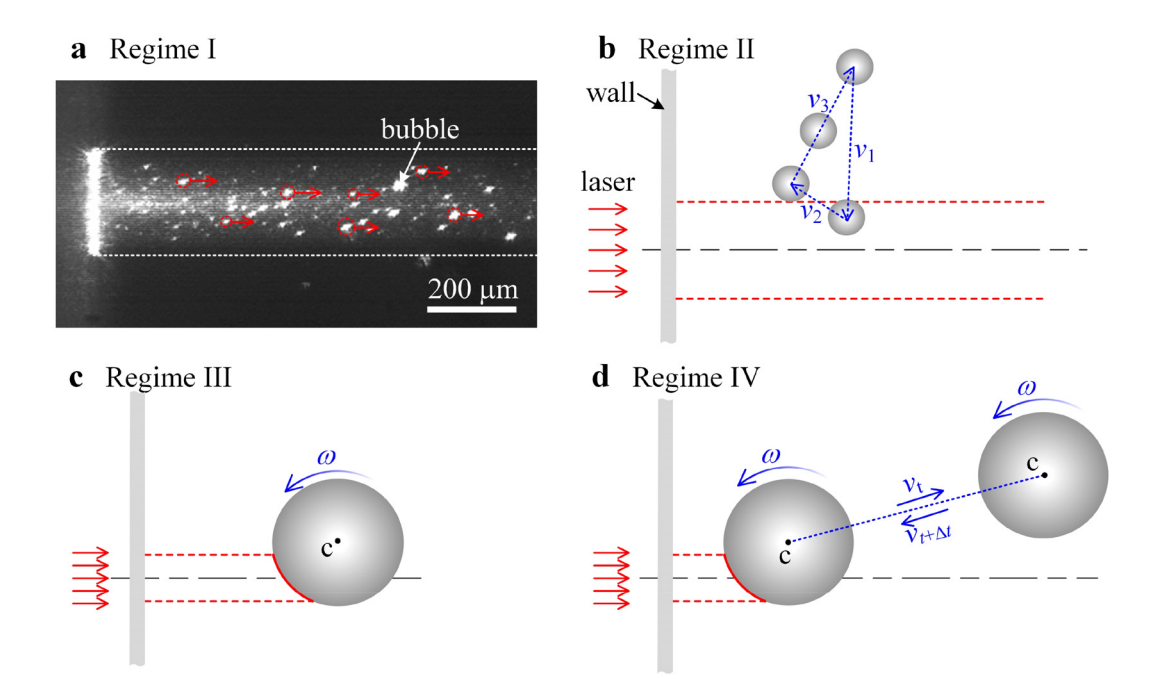


FIG. 2. Four different bubbles flow regimes. (a) Regime I: the micro-bubble stream. (b) Regime II: the laser-frequency-controlled bubble orbital motion and the bubble move along a triangular path. (c) Regime III: the bubble self-rotation motion, in which the bubble hovers in the liquid and self-rotates. (d) Regime IV: the bubble translational motion with self-rotation.

The Marangoni force $F_{\rm m}$ is caused by the temperature gradient on the bubble interface. In nanofluids, laser energy is converted into heat by the nanoparticles, which creates a localized high-temperature region in the laser beam. This causes a temperature gradient in the nanofluid with the temperature decreasing gradually from left to right along the laser beam and decreasing vertically both upwards and downwards from the beam. The bubbles experience Marangoni forces in two directions. In the horizontal direction, $F_{\rm m,\ x}$ acts to the left and is calculated by 30

$$F_{\mathrm{m},x} = -\frac{8\pi r_{\mathrm{b}}^2}{3} \frac{\mathrm{d}\sigma}{\mathrm{d}T} \left| \frac{\mathrm{d}T}{\mathrm{d}x} \right|_{x}. \tag{1}$$

In the vertical direction, $F_{m, y}$ is calculated by

 $3 \quad \text{d} I \mid \text{d} x \mid_{x}$

$$F_{\text{m},y} = \pm \frac{8\pi r_{\text{b}}^2}{3} \frac{d\sigma}{dT} \left| \frac{dT}{dy} \right|_{y}.$$
 (2)

Its direction depends on the temperature gradient around the bubble.

Indirect light pressure F_i arises from non-equilibrium evaporation at the bubble interface.³⁰ When a laser irradiates a bubble, part of it remains within the beam due to buoyancy. The bubble interface is divided into a sunlit side (facing the laser) and a shadowed side (opposite it), as shown in Fig. S2. On the sunlit side, nanoparticles in the overheated boundary layer absorb laser energy, vaporizing the surrounding water and causing bubble growth. The shadowed side absorbs less energy due to the shadowing effect. This creates a heat

TABLE I. The four regimes of laser-induced bubble movement in nanofluid.

Regime	d _{b,ave} (μm)	$\Delta x_{\rm c}$ (μ m)	$f_{\text{o, x}}$ (Hz) $/\omega$ (rad/s)	$\Delta y_{\rm c} (\mu {\rm m})$	$f_{\text{o,y}}$ (Hz)	$f_{\rm l}$ (Hz)	Characteristics
I II	<17.8 48.0–177.4	 16.9–65.0	 50–500	21.8–115.7	50–500	50–2000 50–500	Bubble jet flow Laser-frequency-controlled oscillation in both <i>x</i> and <i>y</i> directions
III	39.3–390.2	2.7-113.1	$\omega = 13.1 - 20.3$	2.7-50.9	• • •	800-2000	Bubble floats and rotates in a limited area
IV	106.1–521.0	192.4–1342.1	11–129	2.7-419.5	0–90	100-2000	Bubble exhibits a large amplitude oscillation in the <i>x</i> -direction, accompany with self-rotation

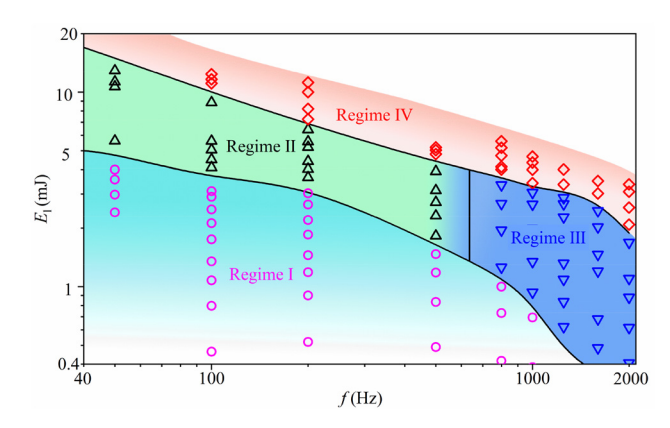


FIG. 3. The bubble flow pattern dependent on single pulse energy $E_{\rm l}$ and pulse frequency $f_{\rm l}$. As the single pulse energy $E_{\rm l}$ increases, the bubble flow regime transitions from the micro-bubble stream (regime I) to the laser-frequency-controlled bubble orbital motion (regime II) or to the bubble self-rotation motion (regime III), and finally to the bubble translational motion with self-rotation (regime IV). The black solid lines between the zones indicate the boundaries and transitions of bubble flow regimes.

flux density q difference between the two sides. As a result, evaporation rates vary across the bubble interface, causing asymmetric bubble expansion. The lower-left hemisphere expands faster than other regions, generating the indirect light pressure. The indirect light pressure is calculated using the following equation:³⁰

$$F_{\rm i} = \nu_{\rm e} \frac{{\rm d}m}{{\rm d}t} + m \frac{{\rm d}\nu_{\rm e}}{{\rm d}t}. \tag{3}$$

Neglecting the effects of the rapid changes in the bubble's radius, $dv_e/dt=0$, it yields

$$F_{\rm i} pprox rac{\pi}{4
ho_{
m g}} \left(rac{q r_{
m b}}{h_{
m fg}}
ight)^2,$$
 (4)

where v_e is the change rate of the bubble's radius and $h_{\rm fg}$ is the latent heat of the water vaporization. The calculation method for q is provided in Ref. 30. The direction of the indirect light pressure F_i is the direction of laser beam propagation.

Frictional drag $F_{\rm f}$ between the bubble and nanofluid results from shear motion in the liquid microlayer at the bubble interface. It manifests as either translational drag or rotational drag, depending on the bubble's movement. The drag force on a translational bubble is given by

$$F_{\rm d} = 6\pi\mu v r_{\rm b},\tag{5}$$

where μ is the dynamic viscosity of the nanofluid. The force is proportional to the bubble's radius and acts in the opposite direction of its motion.

When the bubble rotates, the frictional resistance is given as

$$F_{\rm d} = 8\pi\mu\omega r_{\rm b}^2,\tag{6}$$

where ω is the angular velocity of rotation. The force is proportional to the square of the bubble's radius and opposes the direction of rotation.

C. The flow regimes

1. Regime I: The bubble streaming

In regime I, a large number of micro/nano-sized bubbles form near the wall. These bubbles are confined within the laser beam and rapidly ejected from left to right, as shown in Fig. 4(a) (Multimedia available online). The width of the laser beam is 119 μm . The average power and frequency of the laser beam are 695 mW and 1000 Hz, respectively. As a result of laser heating, the nanoparticles facilitate nucleation within the liquid, leading to the formation of micro-nano bubbles. The laser single-pulse energy $E_{\rm l}$ in regime I is relatively small, and the numerous micro-nano bubbles within the laser beam do not fully grow. The high-speed camera only captures their scattered light.

The motion of the micro-nano bubbles within the laser beam is analyzed [Fig. 4(b)]. The bubble travels within the laser beam in a manner akin to a bullet. Bubble A, as shown in Fig. 4(a), moves rapidly to the right after its formation, with a maximum speed of approximately 98 mm/s, significantly higher than the bubble speeds (~5 mms/s) reported in the literature. For another bubble, bubble B, the maximum speed reaches 110 mm/s. The bubble speed is higher near the laser's incident point, and as the bubble moves away from the incident region (e.g., for $x > 1600 \,\mu\text{m}$), its velocity gradually decreases to approximately 50 mm/s. This is a result of the competitive interactions between the several forces. As presented in Fig. 4(c), in the pulse ON phase, the indirect light pressure acting on the bubbles is greater than the drag force F_d . The indirect light pressure propels the bubbles to move rapidly within the laser beam. Along the laser propagates through the liquid, the laser intension and indirect light pressure attenuation occur, leading to a decrease in bubble velocity [as shown in Fig. 4(b)]. The Marangoni force $F_{m,y}$ exceeds the buoyancy F_b , ensuring that the bubbles remain confined and move within the laser beam. Under laser stimulation, the bubbles are capable of rapidly and directionally transporting payloads to designated locations. This phenomenon holds potential for applications in drug delivery,³⁶ transmission, and artificial intelligence,³⁷ among other fields.

2. Regime II: Laser-frequency-controlled bubble orbital motion

In regime II, the laser pulse energy $E_{\rm l}$ is significantly increased compared to regime I, resulting in the bubble diameter $d_{\rm l}$ reaching the micrometer scale, as shown in Fig. 5(a). The bubble diameters range from 48.0 μ m to 177.4 μ m. Accompanied by the laser ON and OFF, the bubble simultaneously exhibits oscillations in both the vertical and horizontal directions. The bubble's centroid trajectory forms a triangular path. The laser parameters entirely govern the bubbles motion characteristics with the motion frequency identical to the laser pulse frequency.

Figure 5(a) provides a comprehensive depiction of the bubble motion process within two periods. The average power of the laser is 281 mW with a frequency of 50 Hz. At $t=0\,\mathrm{ms}$, and the bubble is above the laser beam when the laser is in the ON phase. The bubble cannot instantaneously change its motion due to inertia. Once the laser ON phase finished, the bubble exhibits an interesting motion trajectory. As illustrated in Fig. 5(b), between 0 and 2 ms, the bubble moves in the lower-left direction at an average speed of 54.9 mm/s. The next 2 ms, it moves to the upper-left at an average speed of approximately

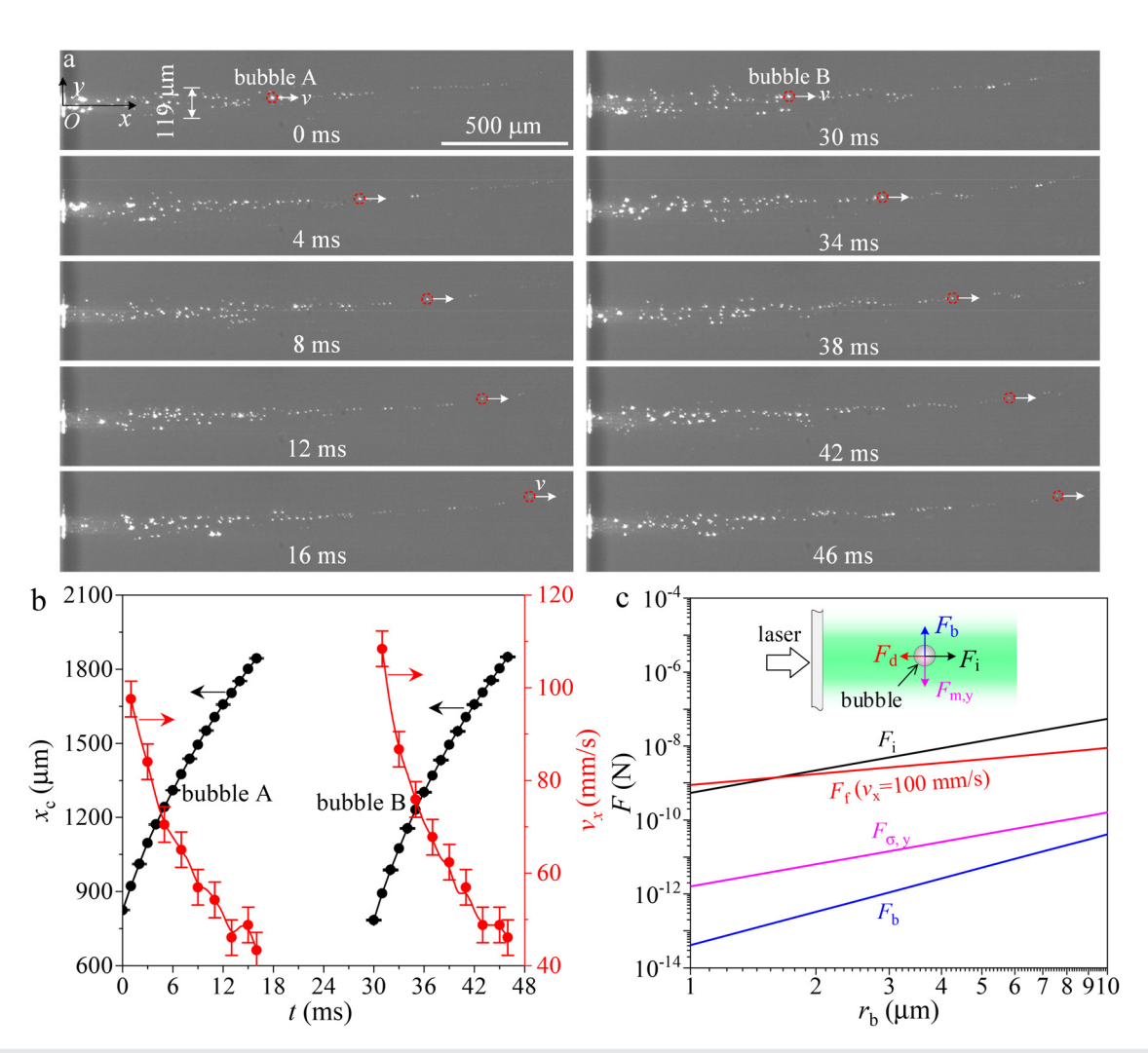


FIG. 4. Regime I: the micro-bubble stream. (a) Bubbles A and B moving to the right within the laser beam. (b) Bubble displacement and average moving velocity as a function of time. The single pulse energy $E_{\rm i}$, pulse frequency $f_{\rm i}$ and laser power P are 0.94 mJ, 1000 Hz, and 0.94 W, respectively. (c) Analysis of bubble force magnitudes with respect to bubble radii. Multimedia available online.

11.1 mm/s. In the remaining 16 ms, the bubble moves to its original point with an average speed of 6.2 mm/s. The trajectory of the bubble centroid from 0 to 20 ms forms a closed triangular path. The temporal and spatial decomposition of the bubble's centroid trajectory is shown in Fig. 5(c). The curves for different coordinate planes reflect the bubbles simultaneous oscillation in the x and y directions with the oscillation frequency matching the laser pulse frequency (50 Hz). The bubble oscillation amplitudes in the x-direction (Δx_c) and y-direction (Δy_c) are 21 μ m and 110 μ m, respectively. The bubble oscillations of this regime are predominantly in the vertical direction. By projecting the centroid motion of the bubble onto the x-y plane, as shown by the red curve in Fig. 5(c), the bubble trajectories from different periods nearly overlap. The bubble motion demonstrates excellent controllability and repeatability, which was manipulated by the laser frequency f_1 and single pulse energy E_1 .

The bubble orbital motion is caused by the periodic variation of the temperature field within the liquid. Figure 6 illustrates the spatiotemporal dynamics of the fluid temperature variations in regime I. Figures 6(a) and 6(c) depict the line distributions of temperature in the vertical and horizontal directions around the bubble at different moments within a bubble motion cycle. Pulse laser, with high instantaneous energy density, intermittently heats the nanofluid. The black curves represent the temperature around the bubble at the laser ON phase. The nanofluid within the laser beam absorbs laser energy, causing the temperature to increase. Conversely, in the laser OFF phase, the absorbed energy dissipates. Comparing the nanofluid's thermal diffusion time and the laser pulse period,

$$\gamma = \tau_{\rm d} f_{\rm l} = \frac{d_{\rm l}^2 f_{\rm l}}{4\alpha_{\rm l}},\tag{7}$$

it yields $\gamma=1.16$, which indicates that most of the heat absorbed by liquid within the laser beam will diffuse outside during laser's OFF phase. The temperature surrounding the bubble undergoes complex fluctuations. The points marked on the curves represent the temperatures at

ARTICLE

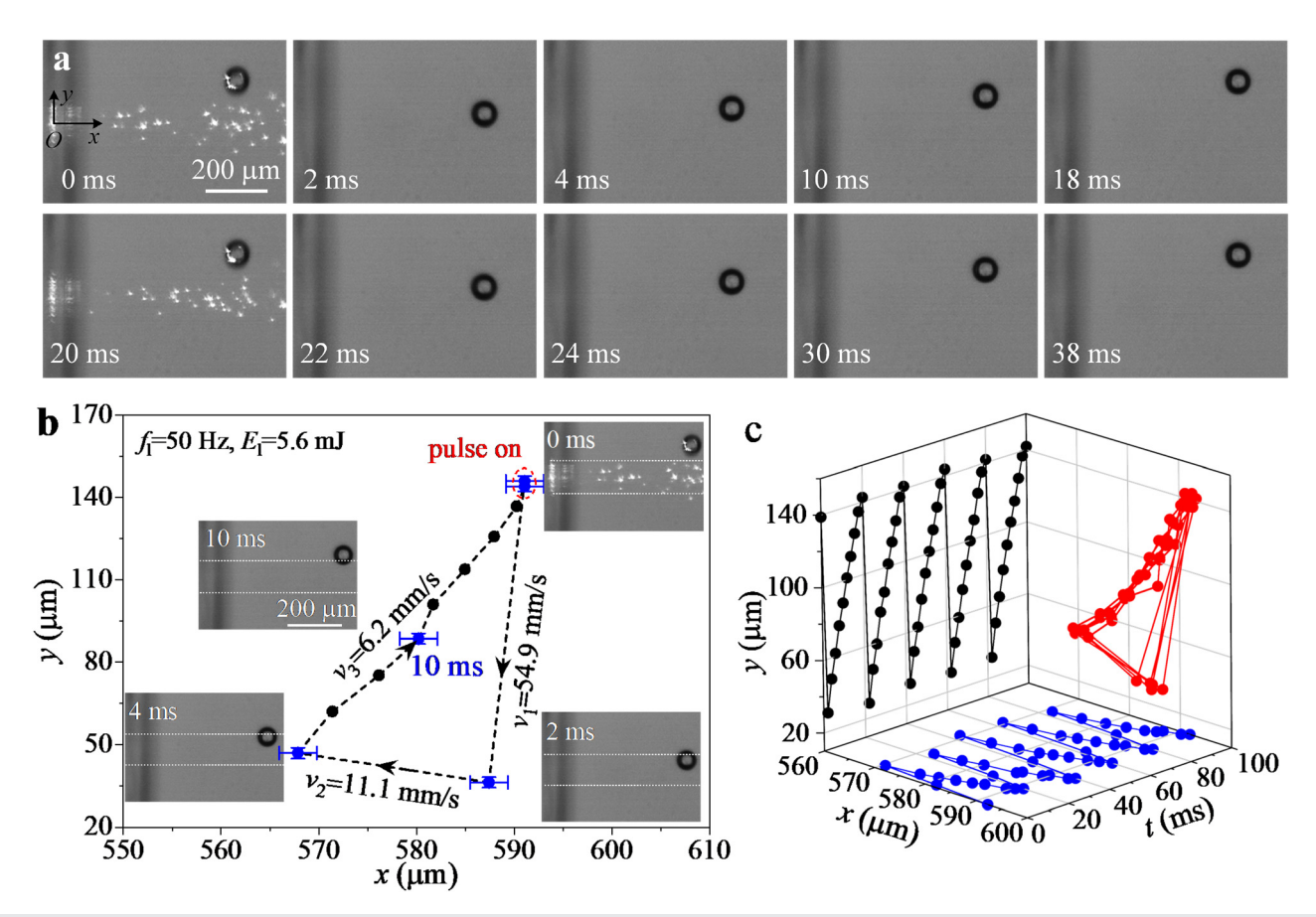


FIG. 5. Regime II: laser-frequency-controlled bubble orbital motion. (a) Bubble moves in liquid with pulse laser ON and OFF. Bubble images with bright images were taken during pulse on, others were taken during pulse off. (b) The bubble's movement process in a single cycle follows a complete triangular trajectory. (c) The bubble's positions in both horizontal and vertical directions at different time points show periodic oscillations. The single pulse energy *E*_I, pulse frequency *f*_I and laser power *P* are 5.6 mJ, 50 Hz, and 0.28 W, respectively. Multimedia available online.

the four apexes of the bubble: top, bottom, left, and right. Figures 6(b) and 6(d) illustrate the variation trends of the temperature differences between the left-right and top-bottom vertices of the bubble, respectively. These temperature differences exhibit periodic oscillations. A positive temperature difference implies that the Marangoni force is greater than zero (cyan zone). Conversely, a negative temperature difference indicates that the Marangoni force is less than zero (pink zone). In the *y*-direction, the direction of the Marangoni force varies continuously in response to temperature changes surrounding the bubble [Fig. 6(b)]. However, in the *x* direction, the Marangoni force remains consistently negative [Fig. 6(d)].

At the laser ON phase, the entire bubble remains above the laser beam and its motion is unaffected by indirect light pressure. The dynamic characteristics of the bubble motion in regime II are governed by the interactions among the Marangoni force, buoyant force, and drag force. Figures 7(a) and 7(b) provide an analysis of the forces acting on the bubble, as well as their relative magnitudes. In the *y*-direction [Fig. 7(a)], during the laser ON phase, the Marangoni force $F_{\rm m,y}$ (negative direction) exceeds the buoyant force, resulting in the bubble's downward motion. In contrast, during the laser OFF phase, the Marangoni force $F_{\rm m,y}$ and buoyant force are of comparable

magnitude, and both forces directed in the positive direction. In the x-direction [Fig. 7(b)], during the laser ON phase, the Marangoni force $F_{\rm m,x}$ exceeds the drag force $F_{\rm d}$, which is arises from the micro-bubble stream flow under indirect light pressure. However, during the laser OFF phase, as the Marangoni force diminishes, the drag force $F_{\rm d}$ slightly slightly exceeds it. To better illustrate the interplay of forces governing the bubble's motion, a schematic diagram [Fig. 7(c)] has been provided, representing the interactions of these forces at different moments within a motion cycle.

At the end of the previous cycle, the bubble is positioned outside the laser beam. Although the liquid within the laser beam undergoes rapid heating during the laser ON phase, the bubble does not move immediately due to the delay caused by heat diffusion and the bubble's inertial resistance to motion. Within the time interval $0 \le t < 2$ ms, the vertical Marangoni force $F_{\rm m,y}$ significantly exceeds the buoyant force $F_{\rm b}$, causing the bubble to move downward into the laser beam over a brief duration, as shown in Fig. 5(b). Simultaneously, the bubble moves slightly to the left under the influence of the horizontal Marangoni force $F_{\rm m,x}$. Once inside the laser beam, where the horizontal temperature gradient is more pronounced, the bubble experiences a substantial horizontal Marangoni force $F_{\rm m,x}$ directed to the left, resulting in

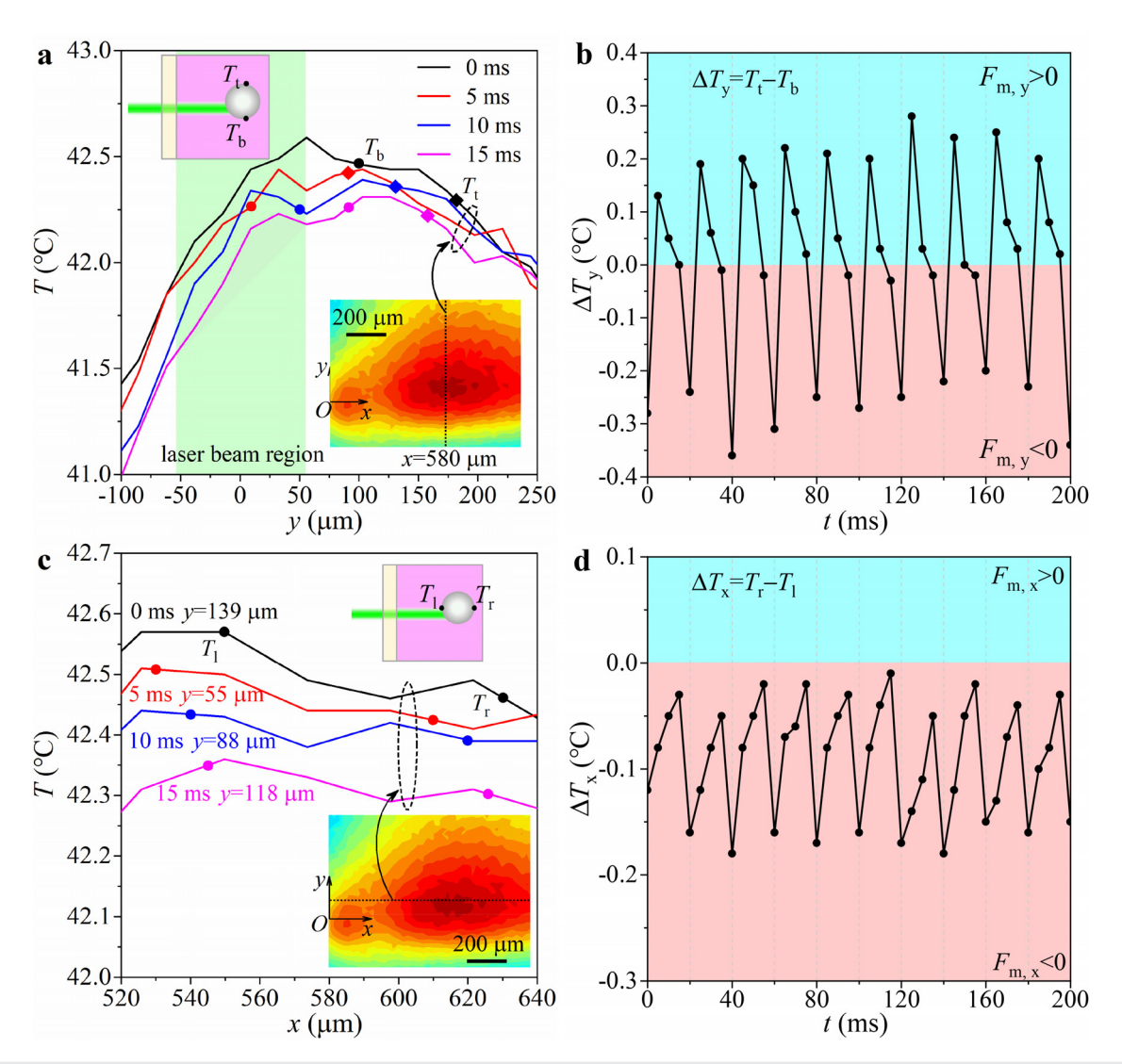


FIG. 6. The temperature distribution of fluid during bubble triangular oscillation. (a) and (c) The temperature distribution at different time points along vertical and horizontal positions, respectively. (b) and (d) The temperature differences at bubble surface vertices in the horizontal and vertical directions over time, respectively. The absolute error of the temperature measurement is $\pm 0.5\,^{\circ}$ C. The cyan zone represents regions where the Marangoni force is greater than zero, while the pink zone indicates regions where the Marangoni force is less than zero. The spatial and temporal temperature variations are critical in understanding the thermal effects on bubble dynamics.

leftward motion during the interval $2 \le t < 4$ ms. At the same time, the combined effect of the buoyant force $F_{\rm b}$ and the vertical Marangoni force $F_{\rm m,y}$, both directed in the positive direction, halts the bubble's downward motion and causes it to move slightly upward. From 4 ms to 20 ms, heat diffusion homogenizes the liquid temperature, weakening the vertical Marangoni force $F_{\rm m,y}$ relative to the buoyant force $F_{\rm b}$. Balanced by the drag force in the vertical direction, the bubble moves upward at a constant speed under the influence of $F_{\rm b}$. In the horizontal direction, the drag force propels the bubble to the right. Consequently, the bubble follows an upper-right trajectory within the liquid. At t=20 ms, the bubble returns to its initial position, thereby completing a full oscillation cycle. Governed by the periodic ON and OFF phases of the pulsed laser, the bubble undergoes a laser-frequency-controlled

triangular orbital motion within the liquid. In other cases of regime II, the bubbles exhibit the same motion process, but the motion amplitude varies depending on the single pulse energy E_1 and frequency f_1 .

The laser frequency serves as a critical parameter in regime II. Based on the preceding analysis and as noted in Table I, the laser frequency f_1 in this regime is relatively low, allowing sufficient time for bubble movement. The long pulse intervals and the supercooled liquid require a higher E_1 to counteract the heat dissipated during the laser OFF phase. As the laser frequency increases beyond 700 Hz, the pulse intervals become too short to allow significant bubble movement, causing the bubble to hover within the liquid and transitioning the flow to regime III. At higher frequencies, the shorter pulse intervals result in

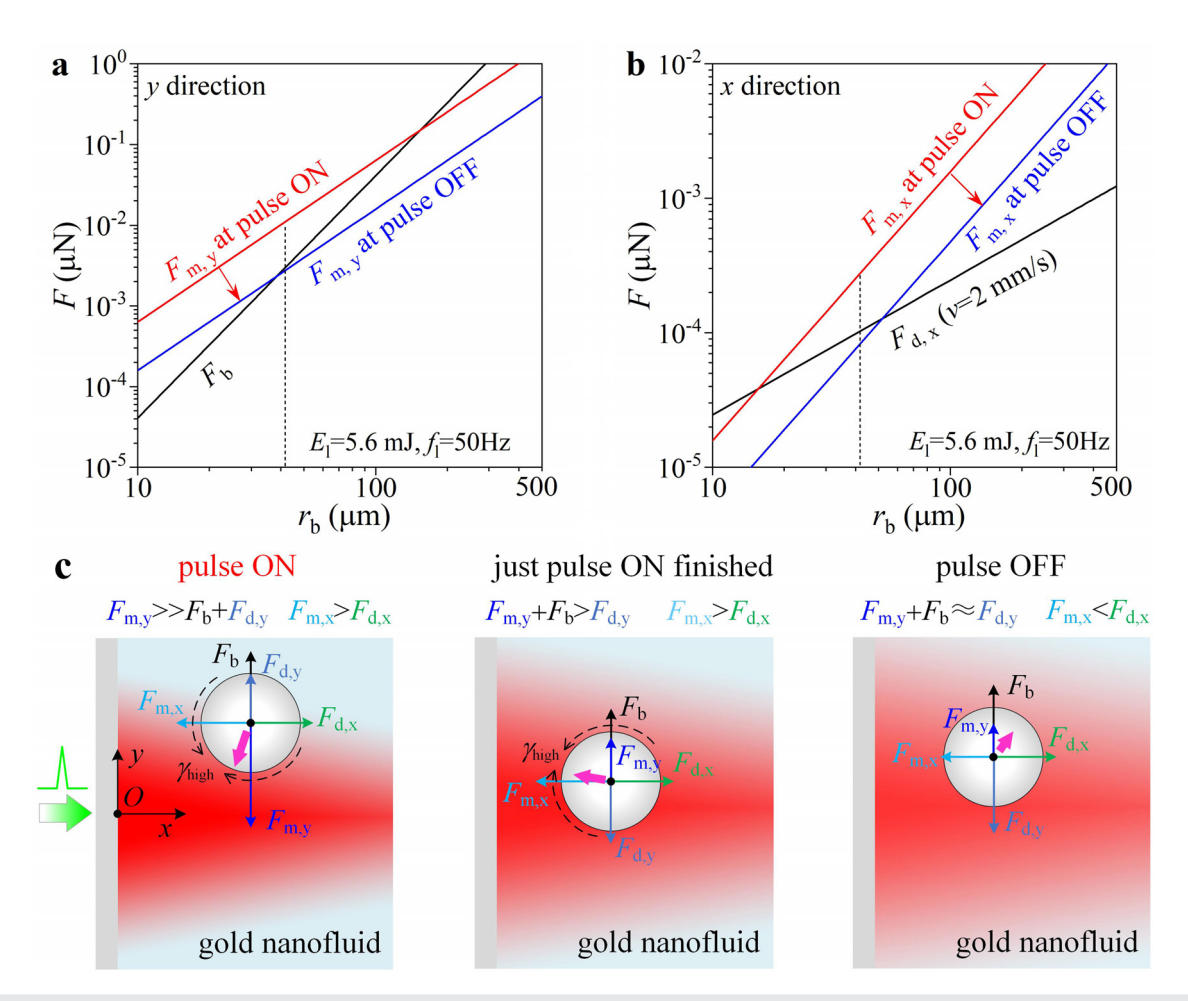


FIG. 7. The force analysis of the bubble in regime II. (a) and (b) The magnitude of the four competing forces during the pulse ON and OFF stages in vertical and horizontal direction, respectively. (c) A schematic representation of the forces acting on the bubble during its motion.

minimal heat dissipation during the laser OFF phase, thereby significantly reducing the $E_{\rm l}$ required to sustain the bubble.

3. Regime III: The bubble self-rotation motion

Figure 8(a) (Multimedia available online) illustrates the bubble self-rotation flow within the liquid. This study is the first to report the phenomenon of bubble self-rotation flow driven by a pulsed laser. The pulse frequency f_l and the single pulse energy E_l are 1600 Hz and 0.70 mJ, respectively. As the laser average power P increases, the bubble diameter enlarges ($d_b \approx 270~\mu m$) and exceeds the laser beam's diameter ($d_l = 119~\mu m$). The bubble's position is considered quasi-stationary due to the small movement amplitude compared to its diameter, as shown in Fig. 8(b). Nonetheless, the bubble does not remain entirely still within the liquid. As evidenced in Fig. 8(a), the bubble rapidly self-rotates in a counterclockwise direction. The bubble self-rotation induces disturbances in the surrounding fluid. In this regime, the pulse frequency is particularly high, rendering the laser OFF phases negligible for the bubble's self-rotation motion.

An impurity was attached to the surface of the bubble, which serves as a tracer marker (point A) to characterize the bubble's rotational state, as shown in Fig. 8(a). The bubble rotates around its centroid with an average angular velocity of 15.2 rad/s. The bubble self-rotates independently, without the support of walls or external objects. The application of laser-driven high-speed self-rotating bubbles holds potential across various domains. For instance, in micro-reactors, the rotating bubble can function as an impeller, enhancing the mixing and reaction kinetics of reactants; in microfluidics, the rotating bubble can facilitate the flow of liquids; and the rotation of the bubble may also be harnessed to develop devices for measuring liquid viscosity.

Previous researchers used moved lasers to produce thermal gradient in liquid inducing the bubble translation motion. 28,29 Marangoni force applied to the bubble act on the bubble centroid and cannot produce the self-rotation moment of the bubble. Different from them, as shown in Fig. 8(a), the laser eccentric irradiation on the bubble causes the bubble self-rotation in this work. The bubble in liquid is affected by the buoyant force $F_{\rm b}$ and the Marangoni force $F_{\rm m,y}$ in the vertical direction, and influenced by the indirect light pressure $F_{\rm i}$ and the Marangoni force $F_{\rm m,x}$ in the horizontal direction. In the

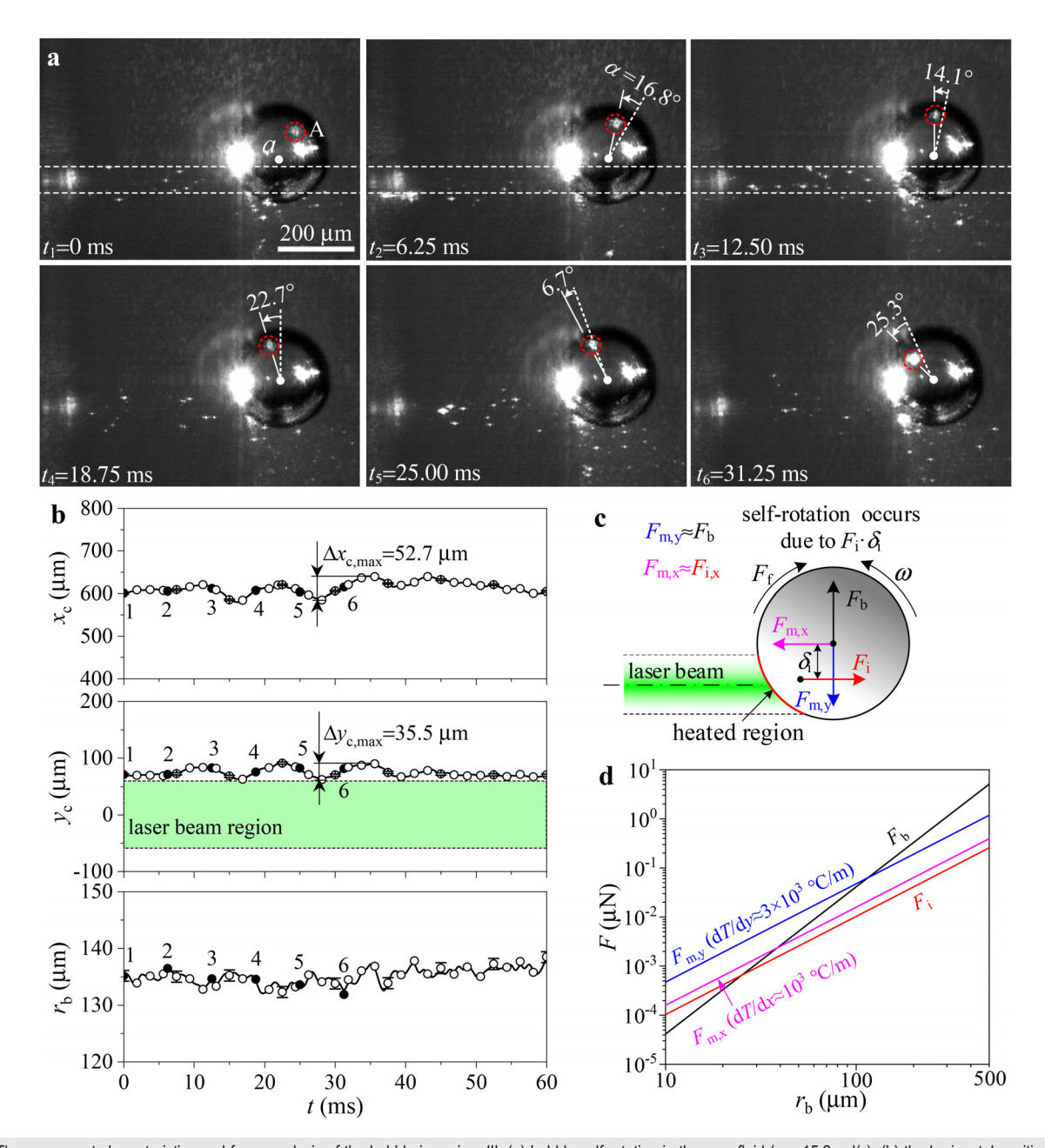


FIG. 8. The movement characteristics and force analysis of the bubble in regime III. (a) bubble self-rotation in the nanofluid (ω =15.2 rad/s); (b) the horizontal position (x_c) and vertical position (y_c) of the bubble center, and the bubble radius (r_b) vs time with the single pulse energy E_l , pulse frequency f_l and laser power P for 0.7 mJ, 1600 Hz, and 1.12 W, respectively. (c) the force analysis of the bubble; (d) the magnitude of four competing forces as a function of bubble radii. Multimedia available online.

circumferential direction, the bubble experiences rotational resistance. The magnitude analysis of four forces acting on the self-rotation bubble are given in Fig. 8(d). The indirect light pressure F_i is the time average value of the pulse period. The temperature gradient on the bubble surface in the vertical direction is significantly greater than that in the horizontal direction, as the top and bottom of the bubble are located outside and inside the laser beam, respectively.

The balance between heat diffusion and laser energy input creates a relatively stable temperature distribution in liquid. The buoyant force $F_{\rm b}$ is balanced by the vertical Marangoni force $F_{\rm m,y}$, resulting in the bubble's stable suspension within the liquid. In the horizontal direction, the horizontal Marangoni force $F_{\rm m,x}$ has a comparable magnitude with the indirect light pressure $F_{\rm i}$. However, the axis of the laser beam does not intersect the bubble's centroid, resulting in a vertical distance

 $\delta_{\rm i}$ between the $F_{\rm i}$ and $F_{\rm m,xo}$ as depicted in Fig. 8(c). This configuration generates a driving torque, $F_{\rm i}$: $\delta_{\rm i}{\approx}8.4\times10^{-13}$ N·m, that induces bubble self-rotation. The rotation of the bubble leads to shear in the surrounding fluid, which exerts a frictional resistance $F_{\rm d}$ on the bubble. Equation (6) yields that the frictional resistance is 4.54×10^{-9} N. The torque resulting from this friction, $F_{\rm d}$: $r_{\rm b}{\approx}6.1\times10^{-13}$ N·m, balances the driving torque, allowing the bubble to rotate stably at high velocities within the liquid. Furthermore, the inherent stability of a rotating object contributes to the maintenance of the bubble's stable suspension in the liquid medium. 41

4. Regime IV: The bubble translational motion with self-rotation

Increasing the single pulse energy $E_{\rm l}$, the bubble demonstrates significant horizontal translational motion accompanied by self-rotation, as illustrated in Fig. 2(d). The characteristic dynamic behavior of the bubble flow regime IV is shown in Fig. 9(a) (Multimedia available online). In this case, the single pulse energy of laser is 4.35 mJ with a pulse frequency of 1000 Hz.

The period of the bubble horizontal oscillation is approximately 65 ms. Figure 9(b) presents the movements of the bubble's centroid in the x and y directions. The bubble moves from left to right in 18 ms, and remains there for approximately 10 ms. Then the bubble returns to the original position over a duration of 37 ms. The bubble takes considerably more time to return to its initial position than it does to move away from it. The maximum horizontal amplitude $\Delta x_{c,max}$ reaches 815.8 μ m, while the maximum vertical amplitude $\Delta y_{c,max}$ is approximately 213.8 μ m. The bubble's radius undergoes expansion and contraction during their oscillation. The bubble's horizontal oscillation frequency is substantially lower than the laser frequency.

The force analysis of the bubble is depicted in Fig. 9(c). The forces acting on the bubble are analogous to those in regime III, when the bubble is close to the laser incident point. As the energy of the single pulse E_1 increases, both the indirect light pressure F_1 and the Marangoni force rise concurrently. However, the increase in F_i is more pronounced. Equation (3) yields that the F_i is attributed to the mass variation and the rapid expansion of the bubble interface. The heat flux density q and the rapid changes in the bubble's radius play a critical role in the F_i . As illustrated in Fig. 9(b), the bubble undergoes rapid expansion, generating a large indirect light pressure F_i that exceeds the horizontal Marangoni force F_{m,x} thereby initiating its movement to the right. The rapid bubble growth results from the cumulative thermal effects of laser irradiation over time and the non-equilibrium heat transfer of the bubble within the liquid. 42 The large bubble blocks the laser propagation. This causes the liquid near the bubble sunlit side to absorb a substantial amount of laser energy. An overheated boundary layer is generated at the sunlit side of the bubble. The thermal energy accumulated in boundary layer rapidly releases, causing the bubble to expand and generate a strong vaporization force that overcomes the vertical Marangoni force $F_{m,x}$ propelling the bubble to the right. The bubble travels a significant distance to the right, accompanied by rotational motion.

During the bubble's rightward motion, the influence of the laser on the bubble and the temperature gradient within the liquid gradually diminish. Consequently, the buoyant force F_b progressively becomes the primary influence on the bubble's motion. The bubble moves upward simultaneously with its rightward motion. When the bubble

reaches its farthest point to the right, the thermal energy within the bubble's thermal boundary layer is fully released, and the bubble is positioned outside the laser beam. At this stage, the bubble is no longer affected by the indirect light pressure $F_{\rm i}$, but the vertical Marangoni force $F_{\rm m,x}$ remains active, driving the bubble back toward its initial location, as depicted in Fig. 9(c). As the bubble moves to the left, $F_{\rm i}$ increases and partially counteracts the horizontal Marangoni force $F_{\rm m,x}$, which results in a deceleration of the bubble's movement. Therefore, the bubble leftward motion is significantly slower than its rightward motion. The bubble flow regime IV is characterized by large amplitude with low frequency, making it suitable for applications such as driving liquid pulsations as a piston 43 or functioning as a bubble heat engine. 30

D. Comments and perspective

In this study, we investigated the dynamic characteristics of bubble motion under pulsed laser irradiation with varying laser parameters. The single laser energies E_1 vary from 0.4 to 15 mJ, and pulse frequency varies from 50 to 2000 Hz. The interplay of Marangoni forces and indirect light pressure results in a variety of dynamic motion regimes for bubbles in liquid (see Table I and Fig. 3). Throughout the experiments conducted in this research, the bubbles were maintained near the laser beam due to the influence of Marangoni forces. For the water-vapor system, bubble motion regimes II, III, and IV encompass oscillation ranges of 48.0-521.0 µm for bubble diameters, $2.7-1342.1 \,\mu m$ in the x-direction oscillating amplitudes, and 2.7-419.5 µm in the y-direction oscillating amplitudes. These parameters are particularly beneficial for optofluidic applications, including mixing, chemical synthesis, and carrier transport, and other processes. In regime II, the bubble self-rotation can be precisely controlled by the laser frequencies. In regimes III and IV, the bubbles are larger than the beam diameter. Notably, in regime III, the bubbles exhibit high-speed self-rotation, which is driven by the dynamic equilibrium of multiple interacting forces. In regime IV, the bubble presents large-amplitude oscillations simultaneously with its selfrotation. The contactless self-rotation of bubbles driven by a laser in liquid has not been previously reported.

This study was conducted using a water-steam system with a laser wavelength of 527 nm. While the observed bubble flow regimes may apply to other working fluids, the flow regime transformation boundaries and suitable laser wavelengths to induce bubble motion are expected to differ. The influence of certain physical properties is discussed herein. Although thermal diffusivity is not explicitly included in the formula of the Marangoni forces, it plays a crucial role in determining the temperature distribution within the liquid, which in turn affects the Marangoni forces in both the horizontal and vertical directions. Fluids with high thermal diffusivity promote a more uniform temperature distribution, diminishing the Marangoni force. Additionally, high thermal diffusivity makes bubble generation more challenging in subcooled liquid. In bubble flow regime II, a high single-laser energy E_1 is required to induce micro-bubble formation and generate a large Marangoni force to trap the bubble. Surface tension also affects the magnitude of the Marangoni force. An increase in surface tension enhances the confinement of the bubble within the laser beam, which reduces the requirements for single pulse energy $E_{\rm l}$. The latent heat of evaporation, $h_{\rm fg}$, is crucial in influencing the indirect light pressure $F_{\rm i}$ [see Eq. (4)]. The utilization of fluids with low h_{fg} significantly increases F_i , thereby enhancing the activity of bubble self-rotation.

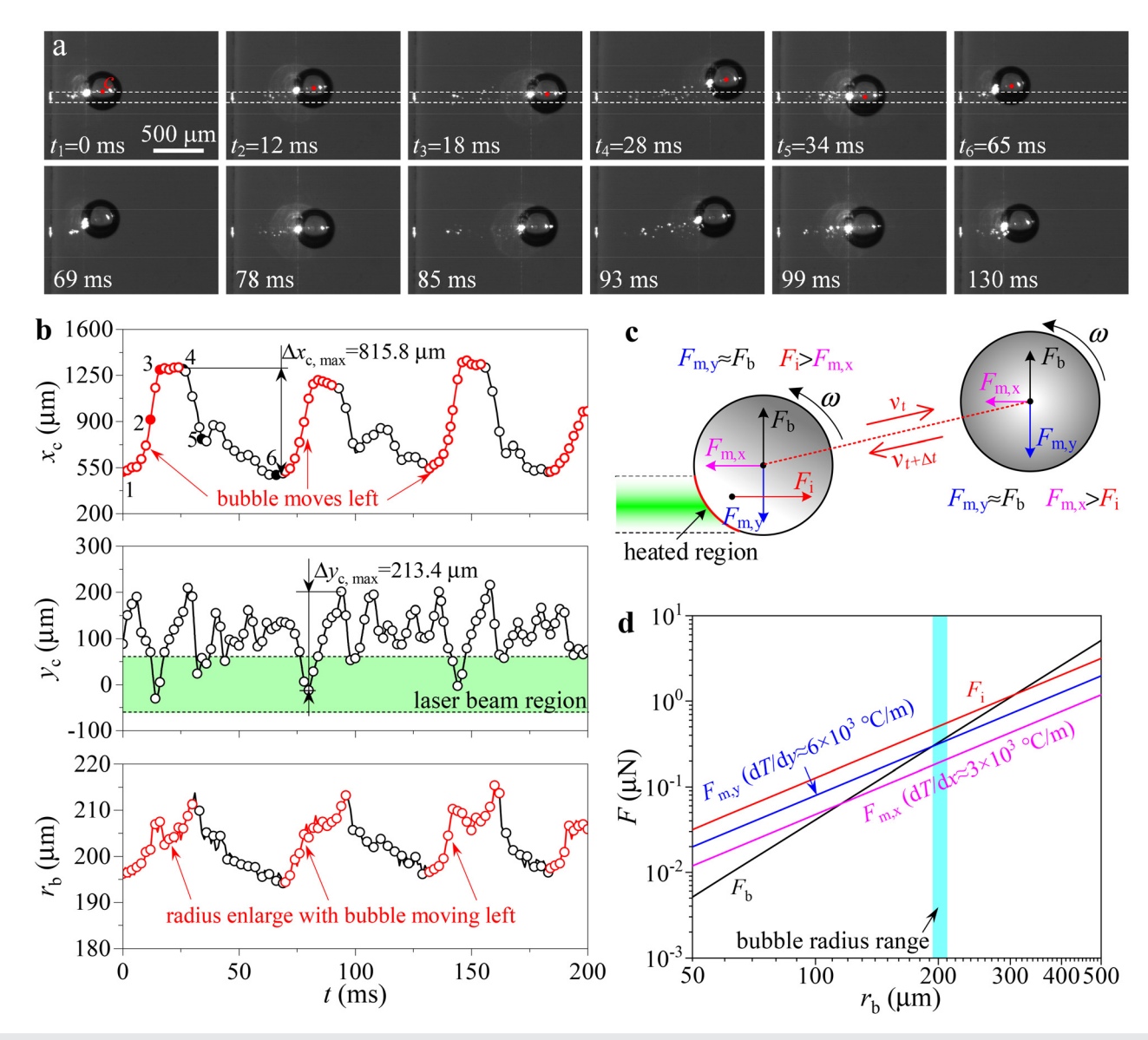


FIG. 9. The movement characteristics and force analysis of a bubble in regime IV. a) the bubble translational motion with self-rotation; b) the horizontal position (x_c) and vertical position (y_c) of the bubble center, and the bubble radius (r_b) vs time with the single pulse energy E_l , pulse frequency f_l and laser power P for 0.44 mJ, 1000 Hz, and 4.35 W, respectively. c) force analysis of bubble during movement; d) the magnitude of four competing forces as a function of bubble radii. Multimedia available online.

Furthermore, fluids with low $h_{\rm fg}$ substantially decrease light energy input to induce bubble formation. Given that the buoyant force is related to the density difference between the liquid and vapor phases, a fluid with a lower density difference decreases the bubble's movement distance in the y-direction in regime II. Consequently, the boundary between regimes II and III shifts to a lower frequency. The wavelength of LSPR for gold nanofluid is 520 nm, as shown in Fig. S1c. Thus, in this study, the laser with wavelength of 527 nm was used to enhance the laser energy absorption and facilitate micro-bubbles generation in subcooled pools. Using a laser with the wavelengths deviating from 520 nm makes it difficult to reproduce the same flow regimes observed

in this study. Similarly, achieving comparable results with other working fluids requires the laser wavelengths matching their resonance.

Finally, we comment on the applications of the bubble flow regimes induced by pulsed lasers. The bubbles achieve orbital motion and self-rotation by simply adjusting the laser parameters without altering the incident point, which is useful in space constrained environments. Compared to the bubble motion dynamics observed with other contactless manipulation techniques, such as acoustophoresis and magnetophoresis, the bubble orbital motion and self-rotation observed in this study not only involve the displacement of the bubbles but also induce self-rotation, thereby enhancing the mass and heat

transfer between the bubble and the surrounding liquid. The bubble interface serves as a medium for the simultaneous presence of gas and liquid phases. By self-assembling reactants at the bubble interface, it is possible to enhance the mixing of different components and accelerate chemical reactions that require the coexistence of gas and liquid phases.³⁸ The bubble self-rotation can also contribute to the development of rotor pumps and novel microvalves,^{44,45} enabling precise control of microfluid transport.

IV. CONCLUSION

This study explores pulse laser induced bubble motion dynamics in a subcooled nanofluid pool. The plasmonic properties of the nanofluids enhance light absorption and plasmonic bubble generation. Varying the laser's single pulse energy (E_l) and frequency (f_l) leads to four distinct bubble flow regimes: micro-bubble streams, laser-frequency-modulated bubble orbital motion, bubble self-rotation flow, and bubble translational motion with self-rotation.

In regime II, bubbles execute rapid triangular orbital motion with amplitudes ranging between 16.9 and 65.0 μm in the x-direction and 21.8–115.7 μm in the y-direction. The bubble motion frequencies match the laser pulse frequency, which governs the characteristics of their orbital motion. In regime III, increasing the pulse frequency causes bubbles to hover and self-rotate, with angular velocities between 13.2 - 20.3 rad/s. The bubble flow in regime IV features large amplitude horizontal oscillations with self-rotation, where bubble diameters vary from 106.1 to 521.0 μm , and oscillation amplitudes range from 192.4–1342.1 μm in the x-direction and 2.7–419.5 μm in the y-direction.

Force analysis indicates that Marangoni forces and indirect light pressure play key roles in pulsed laser induced bubble motion dynamic. Adjusting the pulsed laser parameters modifies the spatiotemporal temperature distribution, which influences the Marangoni forces and indirect light pressure, resulting in various bubble flow regimes. At pulse frequencies below 700 Hz, the Marangoni forces, varying with time and space, drive bubble orbital motion. At higher pulse frequencies, asymmetric laser irradiation induces indirect light pressure, driving the bubble's self-rotation. Increasing the single pulse energy can enhance the indirect optical pressure sufficiently to cause bubble horizontal oscillations. This research provides a comprehensive understanding of the influence of pulsed laser parameters on the bubble motion dynamic characteristics in subcooled liquids, offering guidance for further studies of optically controlled bubble motion using pulsed lasers.

SUPPLEMENTARY MATERIAL

See the supplementary material for Table S1, which summarizes the major parameters, instruments, ranges, and uncertainties; Figure S1, which provides the characterization of gold nanofluid used in experiment; and Figure S2, which illustrates the self-assembly of nanoparticles on the bubble surface and the mechanism of indirect light pressure generation.

ACKNOWLEDGMENTS

The research was supported by the National Natural Science Foundation of China (Grant No. 52306195) and the Fundamental Research Funds for the Central Universities (Grant No. 2023MS026).

AUTHOR DECLARATIONS Conflict of Interest

The authors have no conflicts to disclose.

Author Contributions

Xin Yan: Conceptualization (lead); Funding acquisition (lead); Investigation (lead); Writing – original draft (lead); Writing – review & editing (lead). Jinliang Xu: Project administration (equal); Supervision (equal). Yuqian Zhang: Investigation (supporting). Hongbiao Wang: Data curation (equal); Writing – review & editing (equal). Guohua Liu: Writing – review & editing (equal).

DATA AVAILABILITY

The data that support the findings of this study are available from the corresponding author upon reasonable request.

REFERENCES

- ¹Y. Q. Wang, H. Li, Z. N. Guo *et al.*, "Startup characteristics of long direct-steam-generation loop in parabolic trough solar plant," Renewable Energy **241**, 122390 (2025).
- ²J. Nie, A. Chandra, Z. Liang *et al.*, "Mass accommodation at a high-velocity water liquid-vapor interface," J. Chem. Phys. **150**(15), 154705 (2019).
- ³C. T. Hsiao, A. Jayaprakash, A. Kapahi *et al.*, "Modelling of material pitting from cavitation bubble collapse," J. Fluid Mech. 755, 142–175 (2014).
 ⁴G. Q. Zhou, J. Qu, Z. Li *et al.*, "Next generation flat-plate oscillating heat pipes
- ⁴G. Q. Zhou, J. Qu, Z. Li et al., "Next generation flat-plate oscillating heat pipes characterized by topological channel layouts applicable for multi-heat source cooling," Int. J. Heat Mass Transfer 242, 126869 (2025).
- 51. Xu, W. Zhang, and G. Liu, "Seed bubble guided heat transfer in a single microchannel," Heat Transfer Eng. 32(11-12), 1031–1036 (2011).
- ⁶H. J. Cho, J. P. Mizerak, and E. N. Wang, "Turning bubbles on and off during bubling using charged surfactants," Nat. Commun. 6(1), 8599 (2015).
- 7S. Jung and H. Kim, "An experimental method to simultaneously measure the dynamics and heat transfer associated with a single bubble during nucleate boiling on a horizontal surface," Int. J. Heat Mass Transfer 73, 365–375 (2014).
 8S. Ni, C. K. Cheng, X. R. Li et al., "The hydrodynamic aspect mechanism of the effect of surfactant on boiling heat transfer," Int. Commun. Heat Mass Transfer 156, 107694 (2024).
- ⁹Z. Jia, D. Li, Y. Tian *et al.*, "Early dynamics of laser-induced plasma and cavitation bubble in water," Spectrochim. Acta, Part B 206, 106713 (2023).
- 10 Y. Gao, M. Wu, Y. Lin et al., "Trapping and control of bubbles in various microfluidic applications," Lab Chip 20(24), 4512–4527 (2020).
- ¹¹H. Huang, S. Yang, Y. Ying et al., "3D motion manipulation for micro- and nanomachines: Progress and future directions," Adv. Mater. 36(1), 2305925 (2024).
- ¹²Q. Deng, T. Wu, K. Yin *et al.*, "Efficient anti-frosting enabled by femtosecond laser-induced salt-philic and superhydrophobic surface," Appl. Phys. Lett. 125(12), 121602 (2024).
- ¹³L. Wang, K. Yin, Q. Deng et al., "Wetting ridge-guided directional water self-transport," Adv. Sci. 9(34), 2204891 (2022).
- 14Y. He, K. Yin, L. Wang et al., "Femtosecond laser structured black superhydrophobic cork for efficient solar-driven cleanup of crude oil," Appl. Phys. Lett. 124(17), 171601 (2024).
- 15 A. F. Borkenstein and E.-M. Borkenstein, "Neodymium-doped yttrium aluminum garnet (Nd: YAG) laser treatment in ophthalmology: A review of the most common procedures Capsulotomy and Iridotomy." Lasers Med. Sci. 39(1), 167 (2024)
- procedures Capsulotomy and Iridotomy," Lasers Med. Sci. 39(1), 167 (2024).

 16S. Affan Ahmed, M. Mohsin, and S. M. Zubair Ali, "Survey and technological analysis of laser and its defense applications," Defence Technol. 17(2), 583–592 (2021)
- ¹⁷V. A. Kosyakov, R. V. Fursenko, S. S. Minaev *et al.*, "Physical mechanisms of vapor bubble collapse during laser-induced boiling," J. Appl. Mech. Tech. Phys. **64**(6), 1036–1040 (2023).

- ¹⁸M. B. Li, Y. H. Li, Y. W. Gao *et al.*, "Effect of nanoscale nuclei on the dynamics of laser-induced cavitation," Phys. Fluids 36(9), 093307 (2024).
- 19 J. M. Rossello, H. Reese, K. A. Raman et al., "Bubble nucleation and jetting inside a millimetric droplet," J. Fluid Mech. 968, A19 (2023).
- ²⁰M. Körber, J. Fellinger, M. Fritsche *et al.*, "Ophthalmic surgeries on post mortem porcine eyes with picosecond ultrashort laser pulses," Front. Med. 11, 1345976 (2024).
- ²¹G. T. Bokman, L. Biasiori-Poulanges, B. Lukic *et al.*, "Impulse-driven release of gas-encapsulated drops," J. Fluid Mech. **1001**, A51 (2024).
 ²²H. T. M. Namura, N. F. G. M. C. M. C.
- ²²H. T. M. Nguyen, N. Katta, J. A. Widman et al., "Laser nanobubbles induce immunogenic cell death in breast cancer," Nanoscale 13(6), 3644–3653 (2021).
- ²³G. H. Liu, J. L. Xu, T. Chen et al., "Progress in thermoplasmonics for solar energy applications," Phys. Rep.-Rev. Sect. Phys. Lett. 981, 1–50 (2022).
- ²⁴L. Agiotis, V. T. De Lille, and M. Meunier, "Influence of photothermal and plasma-mediated nano-processes on fluence thresholds for ultrafast laserinduced cavitation around gold nanoparticles," Nanoscale Adv. 5(24), 6887– 6896 (2023).
- ²⁵J. Lombard, T. Biben, and S. Merabia, "Ballistic heat transport in laser generated nano-bubbles," Nanoscale 8(31), 14870 (2016).
- ²⁶J. Lombard, T. Biben, and S. Merabia, "Threshold for vapor nanobubble generation around plasmonic nanoparticles," J. Phys. Chem. C 121(28), 15402–15415 (2017).
- ²⁷L. Mohan, R. Hattori, H. Zhang et al., "Effect of size and interparticle distance of nanoparticles on the formation of bubbles induced by nanosecond laser," Surf. Interfaces 30, 101820 (2022).
- ²⁸Z. L. Wei, H. F. Wang, Y. L. Chen *et al.*, "Microbubble/droplet manipulation based on marangoni effect," Prog. Chem. 36(10), 1541–1558 (2024).
- ²⁹H. N. Li, Y. J. Yang, X. Zhu et al., "Light fueled manipulation of bubble motion against buoyancy via photosensitive substrate," Adv. Funct. Mater. 33(24), 2300308 (2023).
- ³⁰X. Yan, J. Xu, Z. Meng *et al.*, "A new mechanism of light-induced bubble growth to propel microbubble piston engine," Small 16(29), e2001548 (2020).
- ³¹O. V. Angelsky, A. Y. Bekshaev, P. P. Maksimyak et al., "Controllable generation and manipulation of micro-bubbles in water with absorptive colloid particles by CW laser radiation," Opt. Express 25(5), 5232–5243 (2017).

- ³²L. Cheng, Q. Wang, and J. Xu, "Supercritical heat transfer of CO2 in horizontal tube emphasizing pseudo-boiling and stratification effects," Int. J. Heat Mass Transfer 220, 124953 (2024).
- ⁵³C. Zhao, W. An, Y. F. Zhang *et al.*, "Impact of enhanced electric field on light-induced evaporation process of plasmonic nanofluid," Int. J. Heat Mass Transfer 189, 122708 (2022).
- ³⁴K. Setoura, S. Ito, and H. Miyasaka, "Stationary bubble formation and Marangoni convection induced by CW laser heating of a single gold nanoparticle," Nanoscale 9(2), 719–730 (2017).
- 35F. Winterer, C. M. Maier, C. Pernpeintner et al., "Optofluidic transport and manipulation of plasmonic nanoparticles by thermocapillary convection," Soft Matter 14(4), 628–634 (2018).
- ³⁶K. Kooiman, H. J. Vos, M. Versluis et al., "Acoustic behavior of microbubbles and implications for drug delivery," Adv. Drug Deliv. Rev. 72, 28–48 (2014).
- ³⁷L. G. Dai, N. D. Jiao, X. D. Wang *et al.*, "A micromanipulator and transporter based on vibrating bubbles in an open chip environment," Micromachines 8(4), 130 (2017).
- ³⁸S. Surdo, A. Diaspro, and M. Duocastella, "Micromixing with spark-generated cavitation bubbles," Microfluid. Nanofluid. 21(5), 1–10 (2017).
- 39Y. Li, X. Liu, Q. Huang et al., "Bubbles in microfluidics: An all-purpose tool for micromanipulation," Lab Chip 21(6), 1016–1035 (2021).
- ⁴⁰S. C. Lee, J. Heo, H. C. Woo et al., "Fluorescent molecular rotors for viscosity sensors," Chem.—A Eur. J. 24(52), 13706–13718 (2018).
- ⁴¹Y. Dolinsky and T. Elperin, "Stability of particle rotation in a rotating electric field," Phys. Rev. E **79**(2), 026602 (2009).
- ⁴²H. He, L. M. Pan, L. Wei et al., "On the importance of non-equilibrium effect in microchannel two-phase boiling flow," Int. J. Heat Mass Transfer 149, 119185 (2020).
- ⁴³N. Bertin, T. A. Spelman, T. Combriat *et al.*, "Bubble-based acoustic micropropulsors: Active surfaces and mixers," Lab Chip 17(8), 1515–1528 (2017).
- ⁴⁴J.-A. Lv, Y. Liu, J. Wei *et al.*, "Photocontrol of fluid slugs in liquid crystal polymer microactuators," Nature **537**(7619), 179–184 (2016).
- 45J. R. Vélez-Cordero, M. G. P. Zúñiga, and J. Hernández-Cordero, "An opto-pneumatic piston for microfluidics," Lab Chip 15(5), 1335–1342 (2015).